

Award Number: W81XWH-04-1-0551

TITLE: Investigation of Metastatic Breast Tumor Heterogeneity and Progression Using Dual optical/SPECT Imaging

PRINCIPAL INVESTIGATOR: Peter P. Antich, Ph.D.
Anca Constantinescu, Ph.D.
Matthew Lewis, Ph.D.
Ralph Mason, Ph.D.
Edmond Richer, Ph.D.

CONTRACTING ORGANIZATION: The University of Texas Southwestern Medical Center
at Dallas
Dallas, TX 75390-9105

REPORT DATE: May 2007

TYPE OF REPORT: Final

PREPARED FOR: U.S. Army Medical Research and Materiel Command
Fort Detrick, Maryland 21702-5012

DISTRIBUTION STATEMENT: Approved for Public Release;
Distribution Unlimited

The views, opinions and/or findings contained in this report are those of the author(s) and should not be construed as an official Department of the Army position, policy or decision unless so designated by other documentation.

REPORT DOCUMENTATION PAGEForm Approved
OMB No. 0704-0188

Public reporting burden for this collection of information is estimated to average 1 hour per response, including the time for reviewing instructions, searching existing data sources, gathering and maintaining the data needed, and completing and reviewing this collection of information. Send comments regarding this burden estimate or any other aspect of this collection of information, including suggestions for reducing this burden to Department of Defense, Washington Headquarters Services, Directorate for Information Operations and Reports (0704-0188), 1215 Jefferson Davis Highway, Suite 1204, Arlington, VA 22202-4302. Respondents should be aware that notwithstanding any other provision of law, no person shall be subject to any penalty for failing to comply with a collection of information if it does not display a currently valid OMB control number. **PLEASE DO NOT RETURN YOUR FORM TO THE ABOVE ADDRESS.**

1. REPORT DATE 01-05-2007			2. REPORT TYPE Final		3. DATES COVERED 1 May 2004 – 30 Apr 2007	
4. TITLE AND SUBTITLE Investigation of Metastatic Breast Tumor Heterogeneity and Progression Using Dual optical/SPECT Imaging					5a. CONTRACT NUMBER	
					5b. GRANT NUMBER W81XWH-04-1-0551	
					5c. PROGRAM ELEMENT NUMBER	
6. AUTHOR(S) Peter P. Antich, Ph.D., Anca Constantinescu, Ph.D., Matthew Lewis, Ph.D., Ralph Mason, Ph.D., Edmond Richer, Ph.D. Email: PETER.ANTICH@UTSOUTHWESTERN.EDU					5d. PROJECT NUMBER	
					5e. TASK NUMBER	
					5f. WORK UNIT NUMBER	
7. PERFORMING ORGANIZATION NAME(S) AND ADDRESS(ES) The University of Texas Southwestern Medical Center at Dallas Dallas, TX 75390-9105					8. PERFORMING ORGANIZATION REPORT NUMBER	
9. SPONSORING / MONITORING AGENCY NAME(S) AND ADDRESS(ES) U.S. Army Medical Research and Materiel Command Fort Detrick, Maryland 21702-5012					10. SPONSOR/MONITOR'S ACRONYM(S)	
					11. SPONSOR/MONITOR'S REPORT NUMBER(S)	
12. DISTRIBUTION / AVAILABILITY STATEMENT Approved for Public Release; Distribution Unlimited						
13. SUPPLEMENTARY NOTES Original contains colored plates: ALL DTIC reproductions will be in black and white.						
14. ABSTRACT The goal of our project is to image the processes that occur during tumor growth and metastatic spread or regression including the fate of minimal residual disease. To do so it is necessary to test the limits of sensitivity of newly developed techniques: our technical goal is to develop integrated light emission and single photon emission tomography. We have made substantial progress in our techniques for the detection of metastases. We have demonstrated our capability to detect millimeter or sub-millimeter metastases in mice by light emission. To this end we have used Light Emission Tomography (LET), a technique based on bioluminescence of cancer cells infected with luciferase, to detect metastases in the lung and head. We have begun assessment of perfusion using fluorescence imaging. In addition, our technological focus is on the simultaneous use of Single-photon Emission Computed Tomography (SPECT), and to this end we have developed a new form of micro-SPECT based on cooled, electron-multiplied Charge-Coupled Devices (EMCCDs) with which we are performing ongoing imaging experiments. We have also collaborated on the assessment of a new, promising SPECT imaging agent, clioquinol or Iodinated hydroxyquinoline. We will use bioluminescence imaging to test if clioquinol imaging detects areas where tumor cells proliferate and establish metastases and to identify the relative times at which the images first appear.						
15. SUBJECT TERMS SPECT, Optical Bioluminescence Imaging, Metastatic Development, Tumor Heterogeneity						
16. SECURITY CLASSIFICATION OF:				17. LIMITATION OF ABSTRACT	18. NUMBER OF PAGES	19a. NAME OF RESPONSIBLE PERSON USAMRMC
a. REPORT U	b. ABSTRACT U	c. THIS PAGE U	19b. TELEPHONE NUMBER (include area code)			
				UU	26	

Table of Contents

Introduction.....	4
Body.....	5
Key Research Accomplishments.....	8
Reportable Outcomes.....	12
Conclusions.....	15
Appendices.....	17

INTRODUCTION

Because growth of very small tumors has not been studied and documented routinely in detail, this project has increasingly focused on the detection of micro metastases containing fewer than 10^3 cells. The detection of such small tumors would constitute a major advance in diagnosis if extended to the clinical environment.

In our progress to date we have demonstrated our capability to detect sub-millimeter metastases in mice by light emission using Light Emission Tomography (LET), a technique based on bioluminescence of cancer cells transfected with luciferase, and the ability to detect metastases in the entire body of a mouse. We have characterized the procedures which in our hands result most consistently in metastases at different sites.

We have begun assessment of perfusion using fluorescence imaging and will add Nuclear Medicine methods. The question we are currently investigating is, can we reliably detect small tumor foci using techniques that can be more readily translated to the clinical environment? Our technical goal is to compare detection of tumor cells to signals obtainable by Nuclear Medicine techniques.

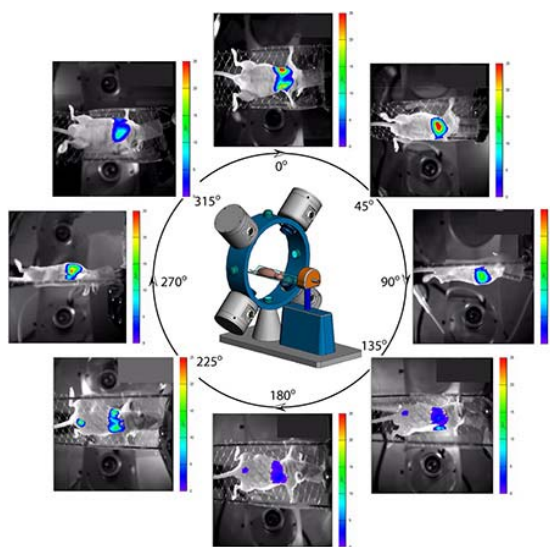
Our technological advances in the simultaneous use of Single-photon Emission Computed Tomography (SPECT) have resulted in a new micro-SPECT based on cooled, electron-multiplied Charge-Coupled Devices (EMCCDs) with which we are starting imaging experiments. Ultimately we plan to use bioluminescence together with SPECT to detect areas where tumor cells proliferate and establish metastases and to identify the relative times at which the images first appear.

BODY

Light Emission Tomography.

Bioluminescence imaging is fast and particularly useful as a screening technique, validated as a high-throughput, quantitative modality for assessing tumor burden, investigating in particular the consequences of different methods of administration of luciferin¹. The simplest form of imaging is non-volumetric, but has several shortcomings⁴⁵: its ineffectiveness in precisely localizing cell populations hampers its use as a visualization tool, while uncertainty in estimation of tumor burden at deep sites impairs its use as a quantitative tool. To obviate these shortcomings while retaining the temporal advantages of planar imaging, we have built a compact multi-camera system to efficiently perform volumetric imaging. We have chosen back-illuminated CCDs (originally Scientific Imaging Technologies Inc., Tigard, OR, now replaced with equivalent CCDs by e2v technologies inc., Elmsford, NY) because of their high quantum efficiency over a broad range of wavelengths (50-95% between 390 and 930 nm).

Currently the system has four cameras, but the number is limited only by cost, complexity and time considerations and can be increased. The four cameras (Figure 1) record simultaneously multiple views of the animal in order to assess the spatial distribution of the emitted light.



Four-camera system for 3D imaging. At each position the cameras record first an image of the animal's surface using reflected light and then a BLI image. The two sets of images are combined for reconstruction. The cameras are then rotated in 18-degree steps using the gantry shown in central panel to obtain sufficient data for high-resolution 3D imaging. In five steps, each camera reaches the position previously occupied by an adjacent camera in order to follow light intensity changes.

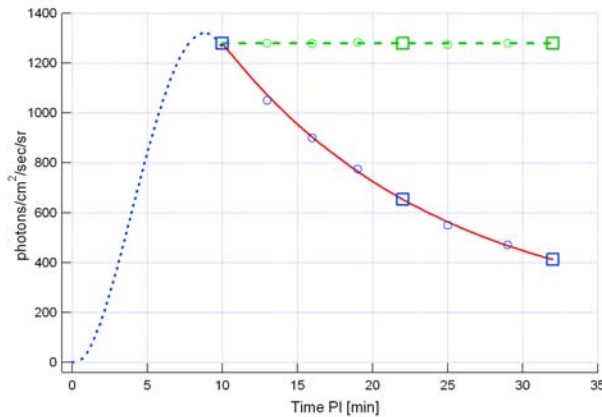
A computer-controlled rotating gantry allows imaging at intermediate angular position to give the extended angular coverage necessary for 3D reconstruction in combination with means we have devised to account for its time variation. For each camera and angle of rotation, we obtain both an image of the animal using external illumination, and an image of internally emitted light. The image of the animal is reconstructed digitally in the same system of coordinates as BLI and is crucial to the process of 3D image reconstruction in our non-contact imaging system. All cameras in the system are calibrated so that the resulting images can be digitally combined. Importantly, the captured light intensity changes by an order of magnitude depending on the angle of detection even though the source intensity remained constant.

Our device overcomes the problems of excessive imaging time with a single camera and the confounding fact that light emission does not remain constant, but changes in time following administration of luciferin (*luc*). The kinetics of light emission depend on numerous factors, such as the location of the cells, physiology, the method of *luc* injection (e.g., IP, IV, SQ or IT), and the

type and concentration of anesthetic ^{1, 14}. With the four cameras in quadrature, proceeding in 18° steps, each camera repeats the measurement of an adjacent camera after five rotations (6 images) to detect changes in light emission.

A multi-camera imaging system is unique in that with sufficient cameras it can capture the light emission from the entire animal surface simultaneously. In addition to reducing the data acquisition time, this innovative approach gives an imaging system that is more robust in handling luciferin kinetics and other time-dependent phenomena that may be present in the imaging data.

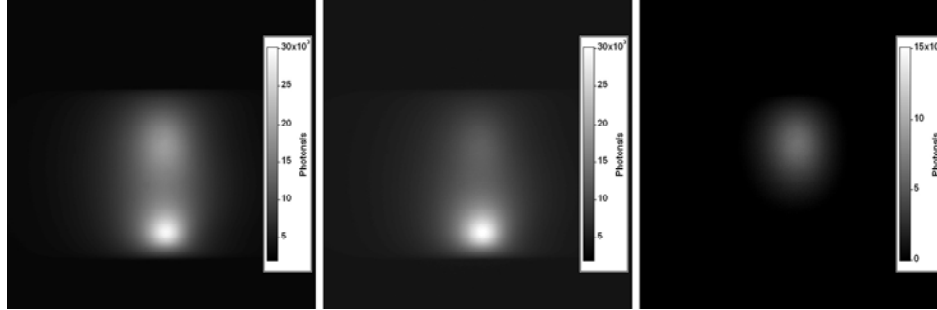
The standard method for correcting tomographic data using rotating camera geometry has been to scale surface intensities obtained at different time points based on an interpolation curve determined from images taken from the same angular direction at the beginning and end of the experiment. The effect is depicted in the figure below, which shows measured and corrected data for a single view.



Time course of light emission after injection of a bolus of luciferin. After reaching a peak at the site of the tumor in 10 min there is a continuous decay of intensity which falls to ½ of its peak value over 10 minutes.

Inherent to this method is an assumption that the luciferin kinetics for all bioluminescent light sources in the animal body is identical. However, we know from pharmacology and drug delivery that luciferin delivery will in fact be heterogeneous and occur at a tissue-dependent rate.

To illustrate the possible effects of site-dependent light emission dynamics, we performed an experiment using 2 point sources located at different depths in a cylindrical, turbid phantom, with one source decaying twice as fast as the other (see below).



Surface light intensity for 2 point sources with different dynamics in a turbid phantom. (left) projection obtained using single rotating camera and corrected using interpolation between baseline and final images; (middle) actual projection collected using synchronous, multi-camera optical imaging system; (right) difference between images, showing that a single camera system is susceptible to errors in data collection for heterogeneous luciferin kinetics.

The image from the single rotating camera (left panel) has been corrected for light emission dynamics using the interpolation method above. In the middle panel, the true surface intensity, as captured by a multi-camera system with complete surface coverage, is shown. The rightmost panel illustrates the error in data acquisition inherent to the single camera/rotating view approach, shown by subtracting the images obtained by the two methods. In this case, the single camera interpolation underestimates the surface intensity from the deeper source. This would undoubtedly lead to errors in depth and intensity in the image reconstruction.]

In summary, we have tested light emission from various sites within the body to determine the circumstances under which we could reliably detect metastases. We developed means to calibrate light intensity in terms of photons/unit area/sec and to evaluate the light intensity emitted by the different cell lines used in our studies. For deeper metastases the light intensity is attenuated and imaging times must be consequently extended.

Changes of emission intensity with time after injection of luciferin. The same head interrogates the same field of view at regulated intervals (squares in figure) and thus our multiple head configuration allows the continuous assessment of changes in light emission. As the different cameras have adjoining fields of view we can monitor these changes and correct their effect on images.

With this technology we were able to detect in vitro with the same instrument extended distributions with 500 cells and foci estimated at 10-30 cells when the cells had sufficient emission intensities. The establishment of reliable models of metastasis to different sites is a prerequisite for our research. To select models which work repeatably in our hands, we performed experiments with different implantation models.

KEY RESEARCH ACCOMPLISHMENTS

Comparison of Cancer Cell Implantation Methods

Bioluminescence imaging experiments were performed using MDA-MB 231 Luc breast cancer tumor cells using different implantation techniques: orthotopic, IV, and intracardiac. The success rate, the time required to form metastatic tumor, and the location of metastases were measured. Bone is a common site of metastasis in human cancer and an animal model that produces such metastases is desirable for research and central to the theme of our project.

1-Orthotopic tumor Implantation

In the case of the orthotopic implantation 40% of the animals developed primary tumors and none developed metastases while the primary tumor progressed. No metastases were detected in a 15 days interval after primary tumor excision in the primary areas of interest, lungs and bone.

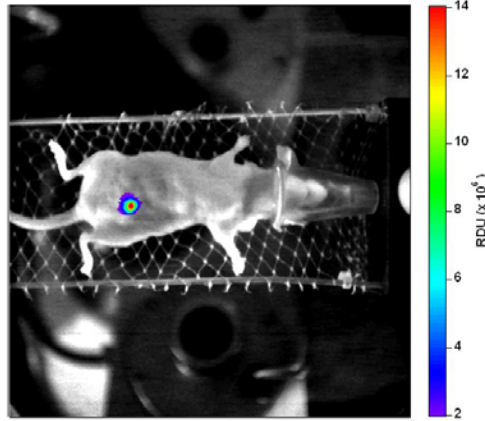


Figure 1. MDA-MB-231 LUC orthotopic tumor. No metastases were detected by 15 days after primary tumor removal.

2-IV

The IV inoculation produced metastases in the lungs of the animal in 60% of the cases. On average the lung tumors could be detected 12 days post injection and they grew at a relatively slow rate.

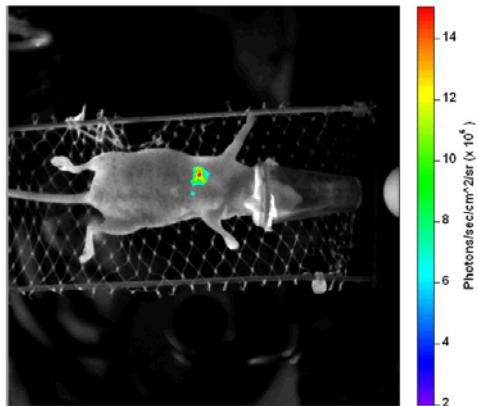


Figure 2. Lung metastases developing after IV injection with 10^6 stably luciferase transfected MDA-MB-231-LUC. They could be monitored and quantified by LET for an average of 90 days.

The rest of the animals (40%) developed metastases in the long bones of the hind legs and in the abdomen. Bone is a common site of metastasis in human cancer, thus this specific animal model is very valuable for research (Fig. 3).

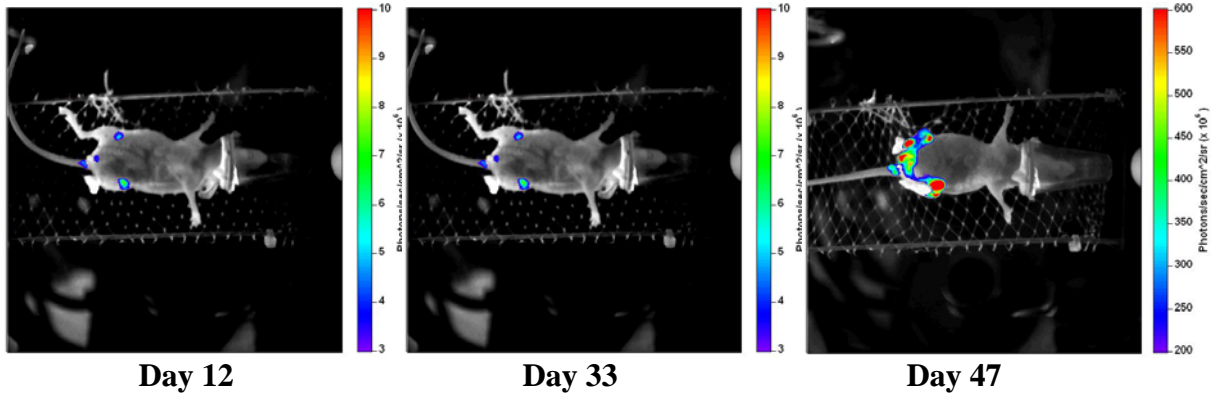


Figure 3. Femoral metastases following IV injection with 10^6 stably luciferase transfected MDA-MB-231-LUC.

3-Intracardiac

A cohort of 8 mice were implanted with MDA-MB-231-LUC cells by injecting them in the left cardiac ventricle. All the animals developed metastases, most of them being localized in the lungs (Fig. 4). The growth rate of the lung tumors was consistent with that of the IV implantation model.

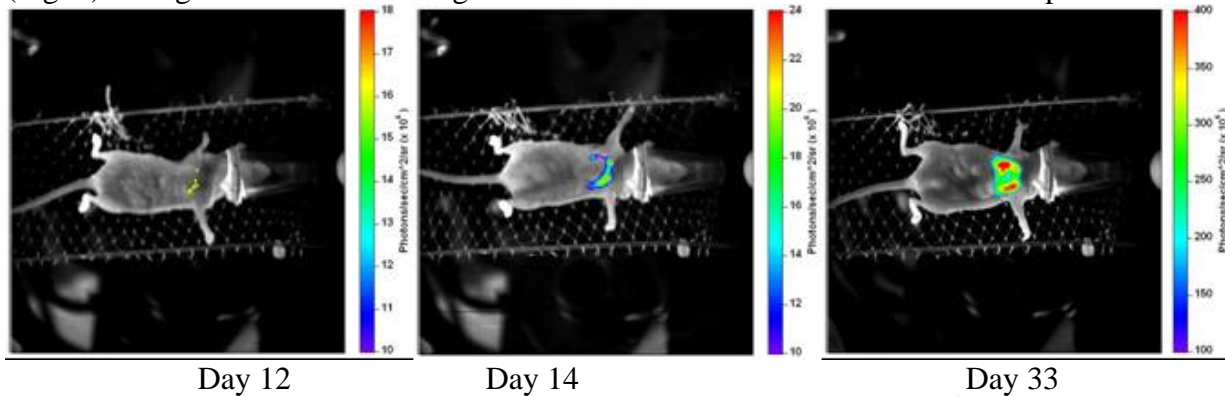


Figure 4. Lung metastases developing after intracardiac injection with 10^5 cells
One animal (1/8) developed metastases in the femur and in the abdominal cavity (Fig. 5).

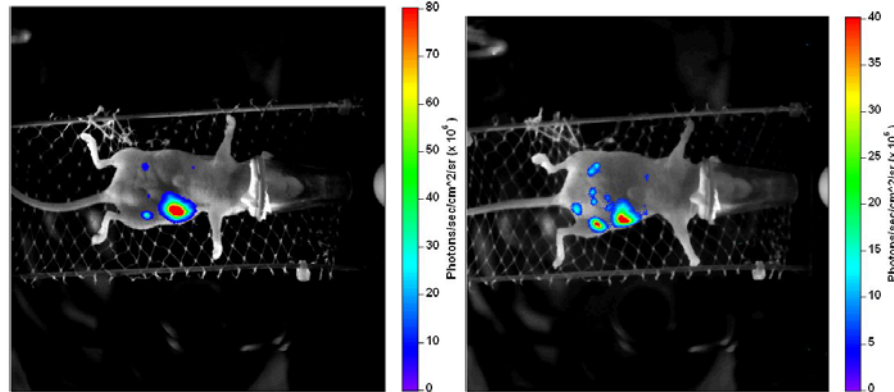


Figure 5. Long bone and abdominal metastases developing after intracardiac injection with 10^5 stably luciferase transfected MDA-MB-231-LUC.

It is important to validate the LET method against other established methods.

Human breast tumor cells (10^6 stably luciferase transfected MDA-MB-231-luc) were injected IV in a nude mouse. The animal was imaged repeatedly by LET and MRI over several weeks as the lung-colonizing metastases appeared and progressed in size and number. Following D-luciferin injection (450 mg/kg, SQ) in the anesthetized mouse, a set of 20 images, 18° apart, was obtained using 1 min exposure starting 5 min post-injection. Data reconstruction provided a 3-D model of the lung tumors. The algorithm was also applied to images obtained using light reflected from the skin under external illumination and the two data sets combined. The imaging time varied from 300 s/angular position for the first imaging sessions that were characterized by low bioluminescent signal, to 30 s/angular position for the later sessions when the bioluminescent signal was large. MRI scans covering the chest of the mouse were acquired on a 4.7 T Varian scanner using a home built respiratory gating unit. We obtained contiguous proton density weighted spin-echo MR coronal slices with the following parameters: TE = 12 ms, FOV= 3.2 cm X 6.4 cm, slice thickness = 1 mm, matrix= 64 X 128 zero filled to 128 X 256, 4 averages. The LET images first detected a bioluminescent signal 22 days after cell implantation, and revealed the growth and spread of the lung metastases at weekly intervals. Tumors in the lungs were first detected by MRI 46 days after inoculation. The smaller tumors from the left lung shown on the LET images were still not observed by MRI. The position and relative sizes of the tumors are consistent between the two imaging modalities. Nevertheless, LET was able to detect the tumors 17 days earlier later than MRI, when the tumors were much smaller.

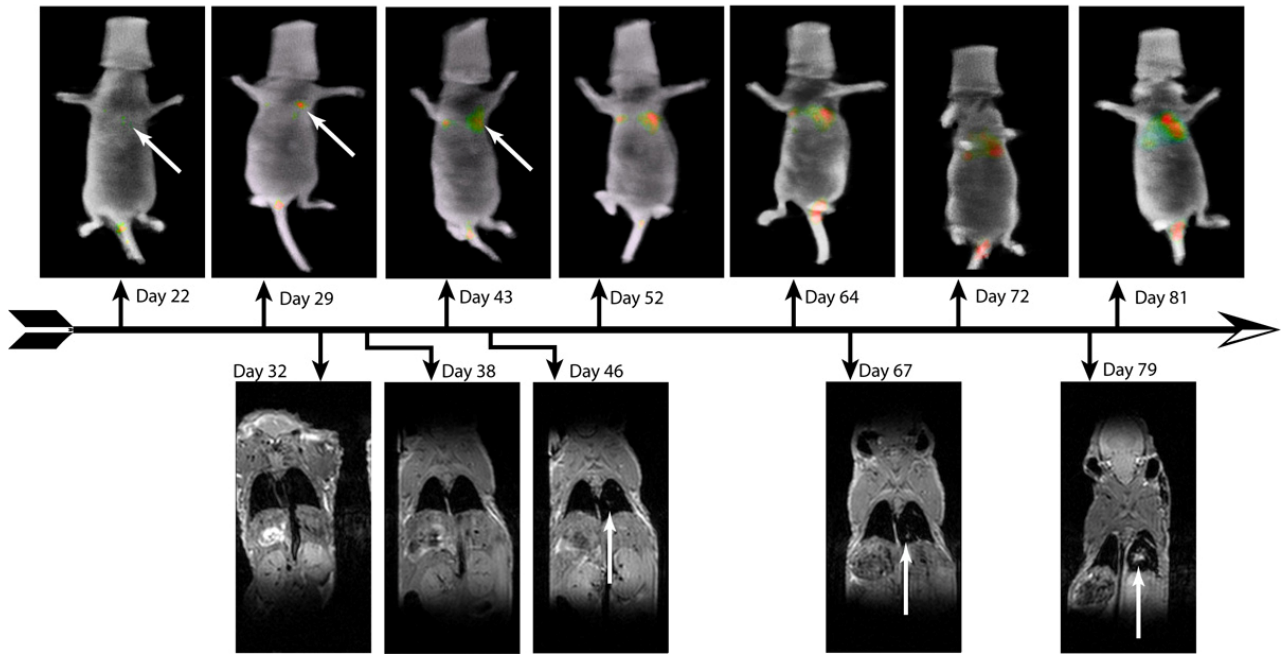
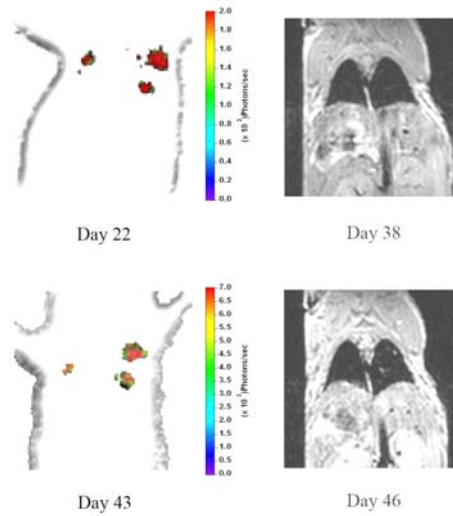


Figure 6. Comparison of metastases detection ability of LET and MRI. Top row shows the LET bioluminescent signal overlay on a 3D reconstruction of the animal surface obtained with external illumination. The anesthesia mask is seen over the nose of the mouse in the reflected light images. Bottom row shows representative slices from MRI scans covering the chest of the mouse, acquired on a 4.7 T Varian scanner.

The figure shows four 1mm-thick tomographic slices, 2 for LET and 2 for MRI.

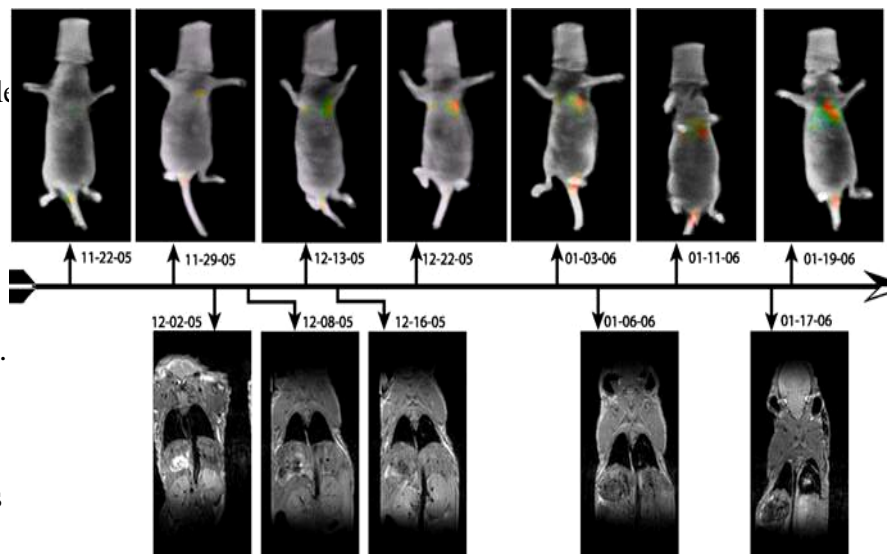
LET shows three metastases on days 22 and 43, two in the left and one in the right lung. Using a 4.5 T small animal magnet, MRI confirms the two metastases in the left lung on day 46. In the LET images the maximum intensity of light emission increases by a factor of 3-3.5 between days 22 and 32.



REPORTABLE OUTCOMES

In a sequential study using the same model the animal was imaged repeatedly by LET and MRI over several weeks as the lung-colonizing metastases appeared and progressed in size and number. Following D-luciferin injection (450 mg/kg, SQ) in the anesthetized mouse, a set of 20 images, 18° apart, was obtained using 1 min exposure starting 5 min post-injection. Data reconstruction provided a 3-D model of the lung tumors. The algorithm was also applied to images obtained using light reflected from the skin under external illumination. The imaging time varied from 300 s/angular position for the first imaging sessions that were characterized by low bioluminescent signal, to 30 s/angular position for the later sessions when the bioluminescent signal was large. MRI scans covering the chest of the mouse were acquired on a 4.7 T Varian scanner using a respiratory gating unit. We obtained contiguous proton density weighted spin-echo MR coronal slices with the following parameters: TE = 12 ms, FOV= 3.2 cm X 6.4 cm, slice thickness = 1 mm, matrix= 64 X 128, 4 averages. The LET first detected a bioluminescent signal 22 days after cell implantation, and revealed the growth and spread of the lung metastases at weekly intervals.

The tumors were first detected by MRI 46 days after inoculation. The smaller tumors from the left lung shown on the LET images were still not observed by MRI. The position and relative sizes of the tumors are consistent between the two imaging modalities. However, LET was able to detect the tumors 17 days earlier than MRI, when the tumors were much smaller.

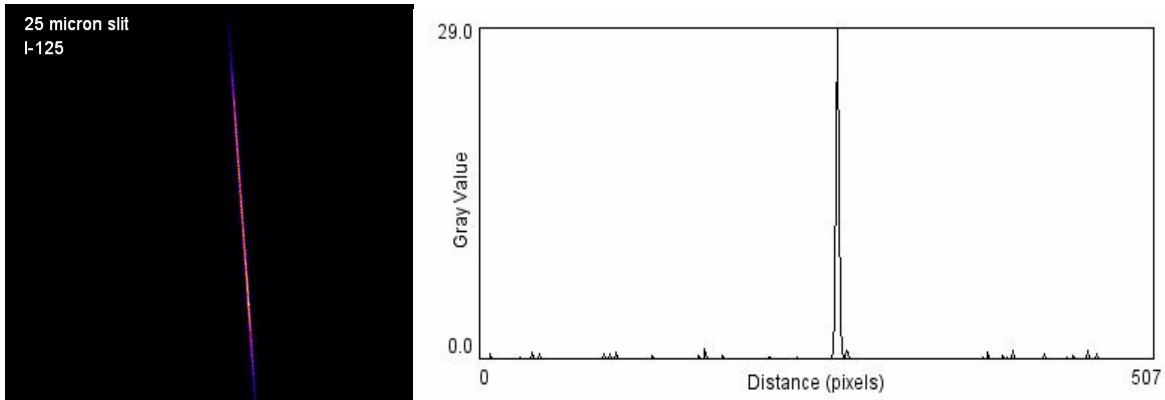


As the tumors developed, the light intensity increased 20-fold. This would permit the study of smaller metastases but to study smaller foci and number of cells it is necessary to adopt higher magnification optics. We are investigating means to do so.

These results validate LET against the powerful MRI 3-D imaging technique. The technique is accurate; in addition it is very sensitive, and studies are in progress to enhance this sensitivity at high resolution and to validate the results with increased statistics.

MICROSPECT

Our project aims at testing multimodality imaging, the second modality being Single Photon Emission Tomography. To this end the CCDs are coupled to scintillating crystals and detect the interactions of gamma rays with the crystal. The complexity of a practical device built using this technique are being studied by a Ph.D. student and the results have been submitted to the IEEE (see attachment).



With appropriate optical means the resolution that can be obtained is high. With I-125 as a source and a 25 μm slit the image has a FWHM of 60 μm .

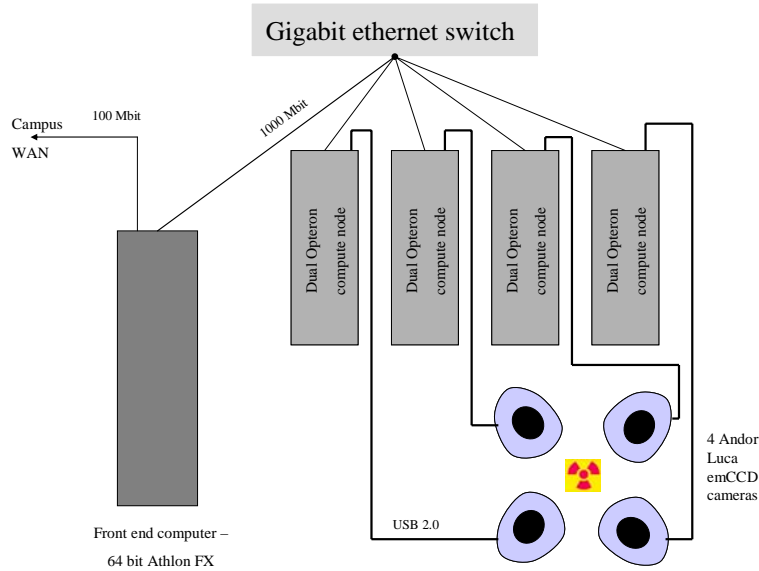
Completion of a small animal SPECT subsystem for this funded effort has been identified as the most important step for the project. Although the original proposal described imaging with iodine-125 labelled agents to obtain the high resolution depicted above, the radiation burden to animals and personnel necessary for obtaining an image is excessive, a decision was taken in the fall of 2006 to use technetium-99m and iodine-123 for small animal imaging. A firm design goal in the 140-159 keV range has facilitated several important engineering decisions.

1.1.1 Selection of camera

Two in-house cameras have been developed for this project. On paper, it was difficult to determine if the Texas Instruments TC253 or e2v CCD 67 would be a better sensor in a lens-coupled gamma camera. The TC253 camera, developed using FPGA methods initiated by this investigator, completed in 2006 by graduate student Todd Soesbe, and submitted for publication in Fall 2006 by him, was discovered to have an undocumented noise floor due to spurious charge generation that was subsequently multiplied in the serial amplification registers. A cooled e2v camera, developed by another sub-team, is not yet available for testing and comparison. Rather than upgrading to the next generation TI TC 247 sensor, it was decided to purchase 4 commercial Andor Luca cameras with this chip. This acquisition was not funded by the project but has made it possible for us to advance more rapidly.



Since multiple USB cameras were not supported by the manufacturer's software, we needed to develop a system for using all cameras simultaneously. Software and methods were developed for converting the Advanced Radiological Sciences Rocks 4.2 computation cluster to a Windows XP based cluster where each node controls an emCCD camera. The computational nodes are connected in a star topology with a frontend through a Gigabit switch, and the system can be rapidly reconfigured from computational cluster to data acquisition cluster.



Depending upon the inserted CDROM, the compute node will install either Linux software for high performance computing or Windows XP and drivers to acquire data from the Andor Luca. Images are published across the high speed network to the frontend where processing, analysis, and image reconstruction will be developed in the future. This high-speed network is private and not accessible from the campus network.

Selection of optics

Due to the conservation of étendue in optics, it is advantageous to minimize the field-of-view on the scintillating crystal. Optical sensitivity is hampered by demagnification. Since the TC247 sensor is approximately 5 mm on a side, we have estimated a 2-3 demagnification factor will be sufficient to obtain projections from a mouse. Numerous optical sensitivity experiments were performed with various lens and lens combinations. We found that a single specific lens with appropriate rings to modulate the field-of-view was the most sensitive.

Selection of scintillator

With a 2-3 cm field-of-view finalized, new crystal scintillators were acquired. CsI(Tl) remains the brightest scintillator with peak emission matched for solid state detectors.

Selection of collimator

Collimator design and fabrication remains a challenge for this project. We have come to believe that pinhole imaging with a high-intrinsic resolution gamma camera is not the best alternative and that it is not feasible to utilize pinholes in the same manner as they are used with PMT-based gamma cameras. Thus a parallel-hole collimator or coded aperture are better suited for small animal imaging.

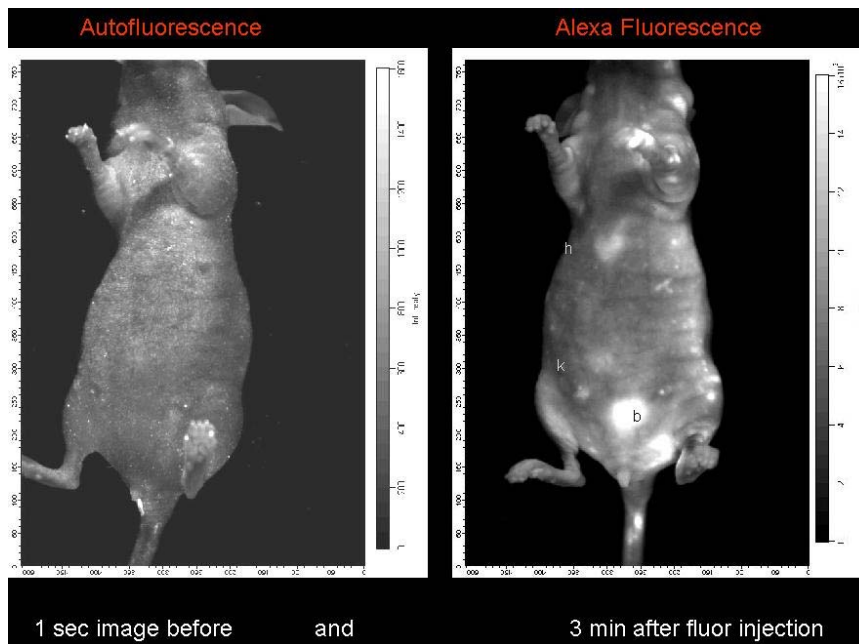
CONCLUSIONS

At present, the four Luca Cameras are mounted on a test platform. Integration on an appropriate gantry -bed system would take less than one week. A new positioning gantry capable of supporting these cameras has been designed and built.

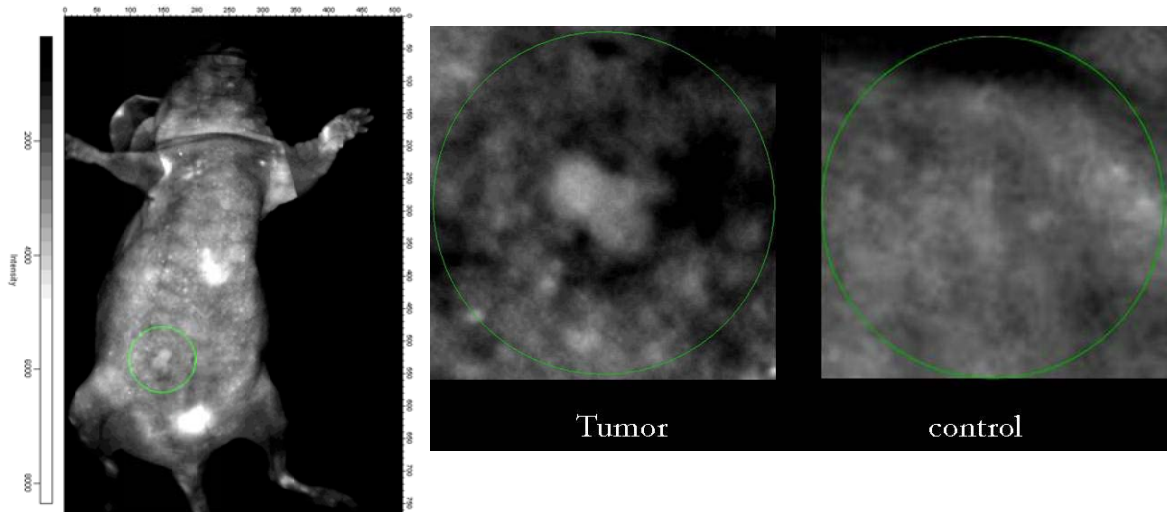
We note that if the LET camera is used to detect the skin of the animal and the SPECT camera is used simultaneously, the perception of the distribution is significantly improved. In the figure below, the MDDP distribution imaged by SPECT identifies active regions of the skeleton.



We note that in addition we can merge bioluminescence with fluorescence imaging. If a dextran tagged with Alexa Fluors is injected in a mouse illuminated in white light, the autofluorescence presents a background signal 14 times lower than the signal produced by the fluor. In the whole body image the prominent light source is the heart as the polymer . Agent washout produces a strong signal in the bladder. is a vascular imaging agent. The were obtained in 1 second.

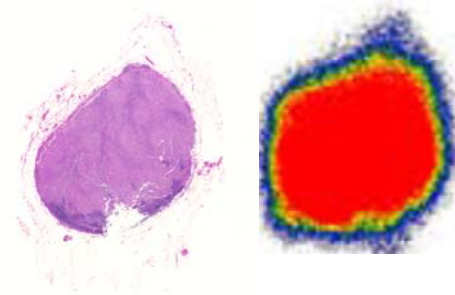


If the same agent is injected in a mouse in which an MDA-MB231 breast cancer tumor grows in the mammary fat pad, a whole body image shows anatomic details as well as the tumor; a higher magnification image reveals the viable tumor against a darker halo around the tumor, produced by absorption of the light used to induce fluorescence by blood vessels and by a dense population of extravasated red blood cells.



Images in fluorescence of a tumor-bearing mouse and perfusion of tumor compared to contralateral mammary. The dark ring surrounding the tumor is formed by necrotic tissue, red blood cells, vascular tissue.

Returning to SPECT, we have participated with our colleagues in evaluating a new imaging agent, Clioquinol. This agent targets areas with high transition metal concentrations. While it was originally developed to image plaque in Alzheimer's disease it is also effective in breast cancer. Thus we show below that the agent stains quite effectively a lymph node metastasis of breast cancer



Lymph node metastasis of CA

The figure shows the radioactivity distribution of $^{125}\text{I-CQ}$ in a tissue slice of lymph node together with a standard tumor stain in an adjacent slice. Intense uptake is shown in red, less intense in blue.



Storage phosphor screen images of BALB/c nude mice injected with $^{125}\text{I-CQ}$: tumor-bearing mouse at right (MDA-435 Human BrCa) vs control at left. The control mouse shows a diffuse distribution but the tumor-bearing mouse shows accumulation in the flank.

APPENDICES

1. Soesbe TC, Lewis MA, Richer E, Slavine NV, Antich PP: Development and Evaluation of an EMCCD based Gamma Camera for Preclinical SPECT Imaging. IEEE Transactions on Nuclear Science, 2007.

Development and Evaluation of an EMCCD based Gamma Camera for Preclinical SPECT Imaging

Todd C. Soesbe, *Student Member, IEEE*, Matthew A. Lewis, *Member, IEEE*, Edmond Richer, Nikolai V. Slavine, Peter P. Antich, *Senior Member, IEEE*

Abstract—The electron-multiplying charge-coupled device (EMCCD) offers improved quantum efficiencies (40 to 95%) over a broader range of wavelengths (400 to 900 nm) and a higher intrinsic resolution ($< 100 \mu\text{m}$ using photon counting) when compared to photomultiplier tubes. The electron gain achieved in the multiplication register of an EMCCD effectively reduces the readout noise to less than 1 electron/pixel, making them sensitive to single photoelectrons. Our prototype camera uses the Texas Instruments Impactron™ EMCCD model TC253SPD-B0 ($7.4 \mu\text{m}$ square pixels) which is cooled under vacuum to -50°C using a four stage Peltier and liquid heat exchanger. Shuttered lens-coupling is used to image the optical light from a 3 mm thick monolithic CsI(Tl) crystal. Precise clocking for the EMCCD is provided by a National Instruments FPGA controller (PCI-7811R) and LabVIEW FPGA module (version 8.0). A custom built electronics box contains the clock driver circuitry and 16-bit video board for digital conversion of the video signal. Our optical coupling method differs from other EMCCD SPECT systems by using lenses rather than fiber optic bundles for transfer. TC253 characterization tests measured a maximum gain just over $1000\times$, dark current rate of 0.14 e/p/s, read noise of 18.2 e/s, and spurious charge generation of 4 e/p. A light integration intrinsic resolution of $110 \mu\text{m}$ FWHM was measured. Light integration images of a line phantom using a single pinhole collimator were used for SPECT reconstruction. We found the relative high spurious charge generation and low quantum efficiency of the TC253 made it incapable of photon counting for low energy sources using lens coupling.

Index Terms—SPECT, preclinical, small animal, EMCCD, gamma camera, pinhole collimator, high-resolution, high-sensitivity.

I. INTRODUCTION

OVER the past decade the demand for high-resolution preclinical (small animal) SPECT imaging has greatly increased. This increase is due to the development of new radiolabeled antibodies, receptor ligands, and other radiopharmaceuticals for both imaging and therapy [1]. The availability of genetically modified mice and *in vivo* molecular imaging for studying gene expression and regulation in human disease has also increased the demand for high-resolution SPECT [2]–[5]. One drawback of previous small animal radiopharmaceutical imaging methods, such as autoradiography, was that several

animals had to be sacrificed in order to achieve significant statistics since each animal could only be measured once [5]. With the development of high-resolution preclinical SPECT, an animal can be measured several times throughout a study, thereby allowing each animal to act as its own control. This leads to fewer animals needed per study, which helps to reduce the overall cost of the experiment.

The small field of view needed to image animals such as mice and rats ($\approx 10 \text{ cm} \times 10 \text{ cm}$) allows for the use of pinhole collimation to achieve sub-millimeter resolution ($< 1 \text{ mm}$ FWHM). Yet the pinhole diameter required for this resolution severely limits the sensitivity of the device. Several methods for increasing the sensitivity of preclinical SPECT systems are currently being pursued. These methods include using multiple single pinhole detectors [6]–[10], multiplexing several pinholes onto a single detector with either minimal [11], [12] or extensive [13], [14] image overlap on the crystal surface, and even using coded apertures commonly found in gamma-ray astronomy [15], [16]. Existing clinical SPECT systems can be modified with pinhole collimators to achieve adequate resolutions for small animal imaging [6], [13], [17], [18], but compact dedicated preclinical SPECT systems can offer higher resolutions and are small enough to fit on a desktop [7].

Another method to improve sensitivity is to use a charge-coupled device (CCD) for the gamma camera photodetector. The application of CCDs to preclinical SPECT imaging has been previously shown by our group [19]. This research has been greatly accelerated by the recent availability of the electron-multiplied CCD (EMCCD) which was first technically described in 1992 [20] and made commercially available in 2001 [21], [22]. EMCCDs combine the positive aspects of photomultiplier tubes (high-gain leading to a high signal-to-noise ratio, photon counting, and energy discrimination) with the positive aspects of CCDs (high quantum efficiencies over a broad spectral range, high intrinsic resolution, and small form factor) making them well suited for preclinical SPECT applications.

Our goal is the development and evaluation of an EMCCD based small animal SPECT device for murine model studies of human disease. Previous applications of EMCCDs to preclinical SPECT imaging mainly use fiber optic bundles to transfer the light from a micro-columnar CsI(Tl) crystal to the imaging area of the EMCCD [25]–[27], [42]. This requires the bundle to be placed very close to, if not touching, the EMCCD surface which creates mechanical, cooling, and vacuum

Manuscript received October 5, 2006; revised April 25, 2007. This work was supported by the DOD BCRP Idea Award Grant W81-XWH-0410551.

T. C. Soesbe is with the Radiological Sciences Graduate Program, M. A. Lewis, E. Richer, N. Slavine, and P. P. Antich are with the Division of Advanced Radiological Sciences at The University of Texas Southwestern Medical Center at Dallas, 5323 Harry Hines BLVD, Dallas TX, 75390, USA e-mail: todd.soesbe@utsouthwestern.edu

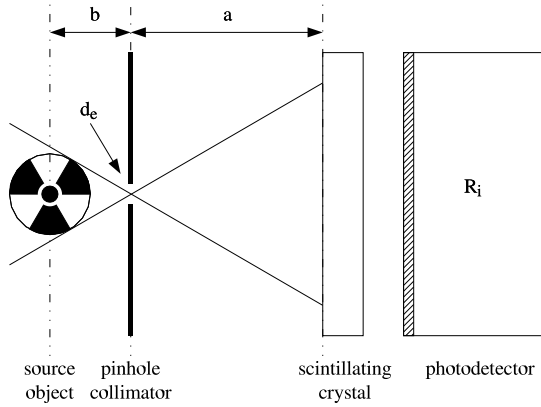


Fig. 1. A schematic showing the geometry of a gamma camera with a single pinhole collimator. When $\frac{b}{a}$ is less than 1, a magnified image of the source object is projected onto the crystal surface.

complications. Our method differs by using monolithic CsI(Tl) crystal and lens coupling for light transfer. With lens coupling, physical contact with the EMCCD is eliminated, although the transfer efficiency is lower compared to fiber coupling. Our approach also differs by using the very low cost Texas Instruments TC253 EMCCD in our custom designed camera. This paper describes the construction of the camera and electronics, EMCCD noise characterization, gamma camera intrinsic resolution, and SPECT reconstruction based on light integration and lens coupling.

II. MATERIALS AND METHODS

A. Spatial Resolution

“Pinhole collimators provide the best combination of sensitivity and resolution for small subjects that are positioned a short distance from the aperture.”

Hal O. Anger, 1967

As seen in the above quote, the advantages of using pinhole collimators to image small source objects that are placed close to the aperture have been known for some 40 years [23]. In fact, the very first gamma camera used pinhole collimation to image the uptake of ^{131}I (364 keV gamma rays) in the human thyroid gland [24]. The setup for a single pinhole gamma camera is shown in Figure 1 where d_e is the effective diameter of the pinhole aperture, b is the distance from the source to the pinhole, a is the distance from the pinhole to the scintillating crystal, and R_i is the intrinsic spatial resolution of the photodetector and scintillation crystal. The total resolution of the system is given by:

$$R_t = \sqrt{\left(d_e \left(1 + \frac{b}{a}\right)\right)^2 + \left(\frac{b}{a} R_i\right)^2} \quad (1)$$

where the first quadratic term under the square root is the geometric resolution (R_g) and the second quadratic term is the effective intrinsic resolution [23]. When $\frac{b}{a}$ is less than 1, a magnified image of the source object is projected onto the crystal surface. This makes the effective intrinsic resolution lower than the intrinsic resolution, which helps to improve the

total resolution. Figure 2(a) shows a plot of R_t , R_g , and $\frac{b}{a}R_i$ versus $\frac{b}{a}$ for $d_e = 1.0$ mm and $R_i = 5.0$ mm, which correspond to the typical pinhole size used in small animal imaging and the typical intrinsic resolution of a clinical SPECT gamma camera respectively. For these conditions, it can be seen that the $\frac{b}{a}R_i$ term quickly becomes the limiting term for the total resolution as $\frac{b}{a}$ increases. As mentioned previously, clinical SPECT gamma cameras can be used for small animal imaging but require large magnification factors to adequately image mice and rats. From Figure 2(a) it can be seen that in order to achieve a total resolution of 1.5 mm with a clinical system, a magnification of $5 \times$ ($\frac{b}{a} = 0.2$) must be used. This leads to large detector surface areas and volumes. In Figure 2(b) d_e is again 1.0 mm but R_i has been reduced by an order of magnitude to 0.5 mm. It can be seen that the geometric resolution is now the limiting term for the total resolution, and that a magnification of only $2 \times$ ($\frac{b}{a} = 0.5$) is needed to achieve a total resolution of 1.5 mm. This greatly reduces the detector surface area leading to a smaller detector volume, which is more suitable for small animal imaging.

B. Pinhole Sensitivity

With a very low intrinsic resolution as in Figure 2(b), the total resolution of the system can be further improved by reducing d_e . Figure 2(c) shows a resolution plot for $d_e = 0.5$ mm and $R_i = 0.5$ mm. It can be seen that R_g is still the limiting term for the total resolution, but now a magnification of $2 \times$ ($\frac{b}{a} = 0.5$) gives a total resolution of less than 1 mm. Although having sub-millimeter resolution is attractive, reducing d_e from 1.0 to 0.5 mm severely reduces the sensitivity (counts/second per source activity) of the system. The on-axis geometric efficiency for a pinhole is given by:

$$g = \frac{1}{2} \left(1 - \frac{1}{\sqrt{1 - \left(\frac{d_e}{2b}\right)^2}} \right) \quad (2)$$

and represents the fraction of emitted photons that pass through d_e from an isotropic point source located a distance b from the pinhole. For $b \gg d_e$ the square root term in Equation 2 can be binomially expanded to give the approximation:

$$g \approx \frac{d_e^2}{16b^2} \quad (3)$$

which is the expression more commonly seen in the literature [7], [17], [23]. When reducing d_e from 1.0 to 0.5 mm, g goes from 0.1% to 0.02% respectively (for $b = 10$ mm). Therefore simply reducing d_e by a factor of two reduces g , and thus the sensitivity, by a factor of five.

One method to increase the sensitivity of pinhole collimation is to simply surround the source object with multiple pinholes. The four main configurations for multiple pinholes are shown schematically in Figure 3, where the first row is the number of pinholes per collimator, the second row is the pinhole configuration, and the third row represents the projected image onto the crystal surface when imaging a uniform planar source. These options include surrounding the source object with multiple single pinhole detectors (a), multiplexing several pinholes onto one photodetector such

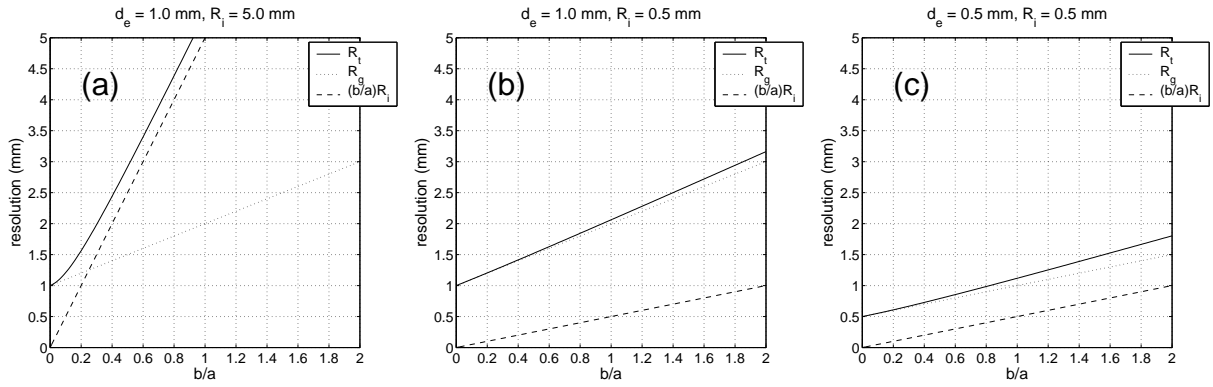


Fig. 2. A plot of R_t , R_g , and $\frac{b}{a}R_i$ versus $\frac{b}{a}$ for (a) $d_e = 1.0$ mm and $R_i = 5.0$ mm, (b) $d_e = 1.0$ mm and $R_i = 0.5$ mm, and (c) $d_e = 0.5$ mm and $R_i = 0.5$ mm. $\frac{b}{a}R_i$ is the limiting term for (a), while R_g is the limiting term for (b) and (c).

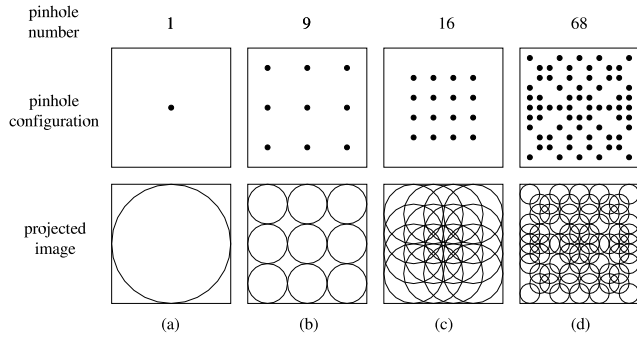


Fig. 3. A schematic showing the four main configurations for multiple pinhole collimation. The sensitivity per collimator increases when moving from left to right.

that there is no image overlap on the crystal surface (b), multiplexing with image overlap on the crystal surface (c), and using a coded aperture which has severe image overlap (d). Although the sensitivity increases when moving from left to right in Figure 3, it is not fully understood how the resolution changes as the image overlap increases and the tomographic reconstruction becomes more complicated. For this project we intend to improve the sensitivity by multiplexing 9 pinholes onto a single EMCCD gamma camera in a non-overlapping manner and surrounding the source with a ring of up to 12 cameras for a total of over 100 pinholes.

C. EMCCD Sensitivity

The sensitivity of a gamma camera system can be further improved by using an EMCCD to detect the optical photons emerging from the scintillation crystal. EMCCDs have higher quantum efficiencies (up to 95% with back-illumination) and broader spectral responses (400 to 900 nm) when compared to PMTs. Also, intrinsic resolutions less than 100 μm have been shown for EMCCD based gamma cameras [25], [26]. The most important characteristic of an EMCCD is the improved low light level signal-to-noise ratio (SNR) when compared to conventional CCDs. This is achieved by the addition of a second serial register, known as the gain or multiplication register, to the CCD architecture as shown in Figure 4.

Electrons are first captured within the pixel potential wells of the image area, then the entire frame (for example 680×500 pixels) is parallel-transferred to the storage area. A single pixel row is then parallel-transferred from the storage area to the serial register. The pixel row in the serial register is then serial-transferred through the multiplication register to the charge-to-voltage output amplifier of the EMCCD. This is done for each row until the entire storage area has been read. The multiplication register differs from the normal serial register by the addition of a third gate known as the charge multiplication gate (CMG) [28]. By making the voltage of the CMG very high (up to 15 VDC) the electrons undergo multiple impact ionization as they move through the multiplication register, which amplifies the electric signal. Although the gain per pixel step is very low (1.01 to 1.018) a multiplication register of 400 pixels in length can allow gains of over $1000 \times$ to be reached [29]. Multiplication of the signal in the charge domain before charge-to-voltage conversion effectively reduces the readout noise of the output amplifier to less than 1 electron/pixel. This eliminates the noise floor found in conventional CCDs making EMCCDs sensitive to single electrons.

The total signal noise of an EMCCD is given by:

$$\sigma_t = \sqrt{G^2 F^2 (P + D + S) + \sigma_r^2} \quad (4)$$

where G is the gain, F is the excess noise (Fano) factor due to the gain process in the multiplication register, and P , D , S , and σ_r are the mean signals (electron/pixel) due to the photon (shot), dark current, spurious charge, and read noises respectively [29], [30]. The dark current noise (D) and the spurious charge noise (S) can be reduced to negligible levels with cooling and proper clocking respectively [31]. Also, for a gain greater than $\approx 10 \times$, F approaches $\sqrt{2}$ [32]. Under these conditions the SNR for a EMCCD reduces to:

$$SNR_{EMCCD} = \frac{GP}{\sigma_t} = \sqrt{\frac{P}{2}} \quad (5)$$

when $G \gg \sigma_r$. This can be compared to the SNR of a conventional CCD under similar condition given by:

$$SNR_{CCD} = \frac{P}{\sqrt{P + \sigma_r^2}} \quad (6)$$

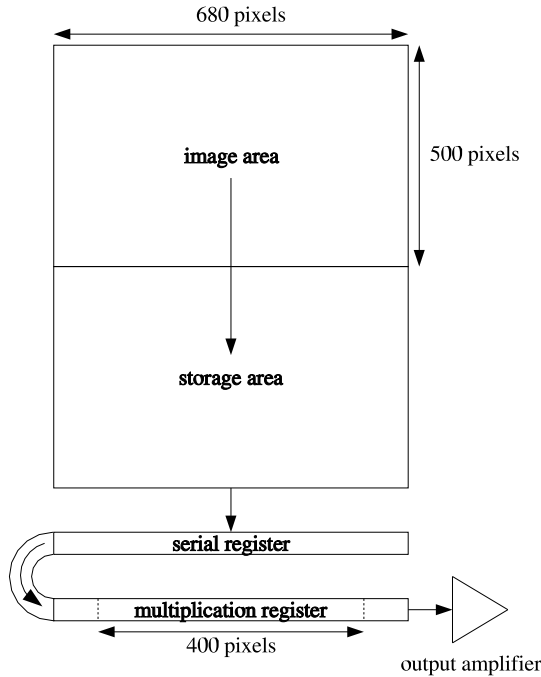


Fig. 4. A schematic showing the architecture of an EMCCD. The electrons are multiplied by impact ionization as they move through the multiplication register before charge-to-voltage conversion in the output amplifier.

A plot of SNR_{EMCCD} and SNR_{CCD} versus P is shown in Figure 5 for a typical read noise ($\sigma_r = 25$ electrons/pixel). It can be seen that while the CCD has a SNR of 1 at 25 electrons/pixel, the EMCCD has a SNR that is 3.5 times higher.

D. Camera Prototype

A schematic of the prototype system is shown in Figure 6. The system consists of a PC with a FPGA card, an external electronics box, and the EMCCD camera assembly. The National Instruments PCI-7811R (Xilinx FPGA, 1 million gates, 40 MHz digital rate, 25 ns resolution) produces the clock pulse timing for the EMCCD. These pulses are sent to the driver board inside the external electronics box which converts the TTL pulses to the proper voltages needed to drive the EMCCD. The driving pulses are then sent through an R/C circuit located inside the camera housing for shaping before entering the EMCCD. The video signal from the EMCCD is first sent through a preamp and then through a video board. The video board uses correlated double sampling (CDS) of the video signal to help reduce noise before digital conversion in a 16-bit ADC (Analog Devices AD976A, 200 kHz max rate). The digitized video signal is then sent back to the FPGA which uses a DMA FIFO across the PCI bus to store the data on the host computer which is running LabVIEW 8.0.

For the prototype camera we used the Texas Instruments Impactron™ TC253 EMCCD chip (TC253SPD-B0). This front-illuminated chip (35% quantum efficiency at 560 nm) has $7.4 \mu\text{m}$ square pixels (100% fill factor) in a 680×500 , 1/3 inch format. The TC253 has a nominal read noise of

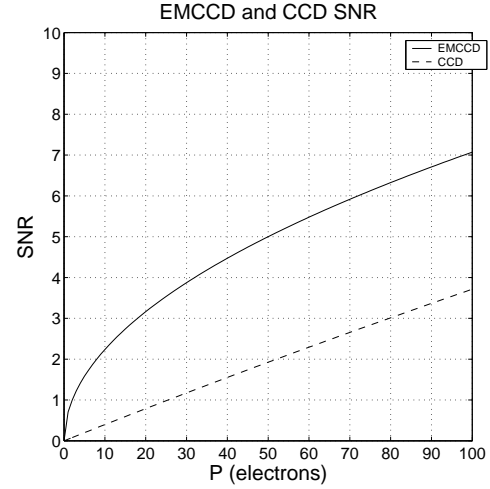


Fig. 5. A plot showing the EMCCD and CCD SNR as a function of electrons/pixel. The EMCCD SNR is much higher for low light level imaging.

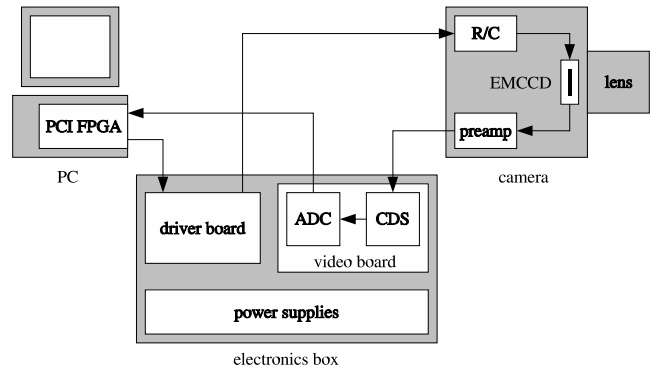


Fig. 6. A schematic showing the setup for the prototype EMCCD camera.

29 electrons/pixel RMS at video rate readout (12.5 MHz clock frequency). It also has low dark current generation (≈ 0.1 electron/pixel/sec at -40°C) and a built in single stage Peltier element capable of cooling the chip down to -10°C . Figure 7(a) shows a close up photo of the TC253. The TC253 is mounted onto an Aluminum cold-finger which sits on top of a four-stage Peltier element. Low thermal conductivity wires connect the TC253 to the R/C and preamp circuitry with all camera electronics being contained in the vacuum housing. Figure 7(b) shows an exploded view of the camera assembly showing the lens, shutter, vacuum window, EMCCD housing, and a choice of either air or liquid heat exchanger. A picture of the assembled camera is shown in Figure 7(c).

III. RESULTS

High quantum efficiency back-illuminated EMCCDs such as the e2v CCD97 currently cost between 6k to 7k USD. Off-the-shelf camera systems containing these EMCCDs such as the PhotonMAX 512B cost around 30k USD. To increase the sensitivity of our preclinical SPECT system, we would like to surround the animal with a ring of multiple cameras. Therefore, in order to reduce the cost per camera to a reasonable level, we have opted to design and build our own. By using

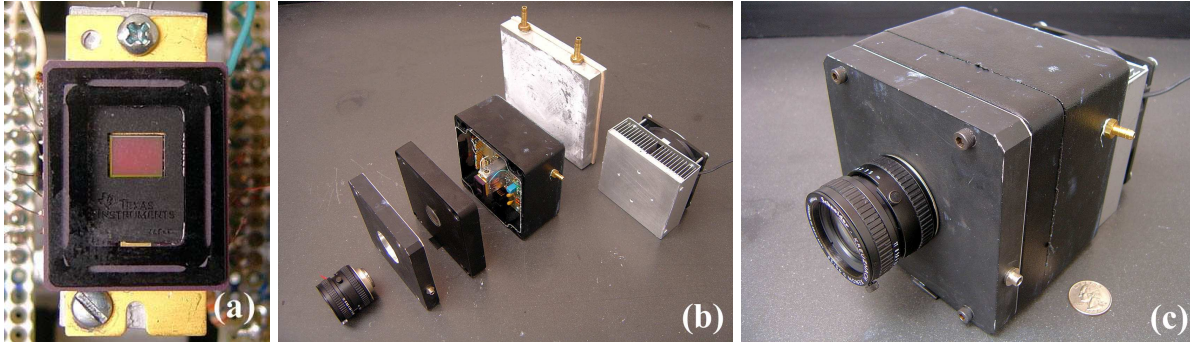


Fig. 7. (a) A photo showing the front face of the Texas Instruments Impactron™ TC253 EMCCD mounted to the Aluminum cold finger. The image area (680 × 500 pixels) measures 5.0 mm × 3.7 mm. (b) An exploded photo of the camera assembly. (c) The assembled camera with air heat exchanger.

the low-cost front-illuminated TC253 EMCCD (500 USD), the PCI-7811R FPGA card with LabVIEW module (2k USD), and custom built electronics (500 USD), the cost per camera is reduced by an order of magnitude to 3k USD. Details of the camera system, followed by TC253 noise characterization, and initial light integration imaging results are presented next. Although the system has a gain of over 1000×, low read and dark noises, and good intrinsic resolution, the relative high spurious charge generation and low quantum efficiency of the TC253 make it incapable of photon counting for both ^{99m}Tc and ^{125}I using monolithic CsI(Tl) crystals with lens coupling.

A. EMCCD Characterization

Upon completing the prototype camera, we first characterized the EMCCD by measuring the gain, dark current accumulation rate, total read noise, and spurious charge generation to verify that they were within the specified operating range of the TC253. Methods and results for the measurements are described here. All measurements were taken at $-40\text{ }^\circ\text{C}$.

1) *Gain*: The gain versus positive charge multiplication gate voltage (+CMG) of the TC253 was measured using lens coupling to image a controlled light source. The light source consisted of a 3 mm green LED embedded in a 10 mm × 15 mm Teflon cylinder to create a small diffuse uniform source that was viewed on end. With the EMCCD gain set to 1 (+CMG = 7.0 V), the current to the LED was varied until a SNR of about 5 was achieved for an average of 1000, 33 msec exposures. The difference between the dark reference pixels and peak signal was measured using a line profile of the averaged image. This measurement was repeated as the +CMG voltage was increased, with the increase between the dark and peak pixels being taken as the gain. A plot of gain versus +CMG is shown in Figure 8. It can be seen that the gain starts to increase past 11 V and rises to over 1000 at 14 V.

2) *Dark Current*: Dark current arises from thermal generation of electrons within the silicon lattice of the EMCCD. These electrons are captured by the pixel potential wells and contribute to the non-photon related signal noise (see Equation 4). Dark current generation is proportional to exposure time, independent of the amount of light incident on the EMCCD, and can be significantly reduced by cooling [33]. The dark current accumulation rate for the TC253 was measured

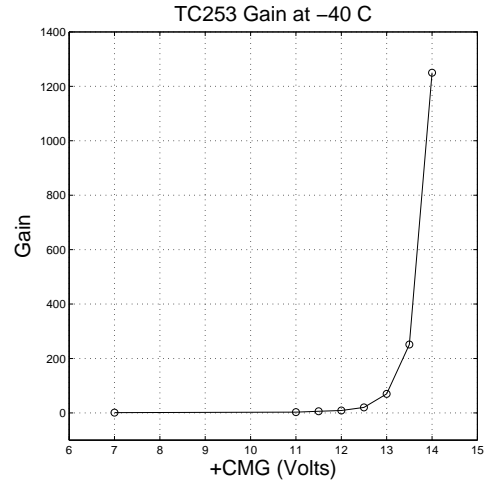


Fig. 8. A plot of EMCCD gain versus positive charge multiplication voltage (+CMG) for the TC253. A gain of over 1000× is reached at 14 V.

by taking N exposures at a fixed dark exposure time. The mean and standard deviation of the N exposures were then calculated for each pixel. The ensemble average of the pixel means over the active EMCCD area was taken as the dark current count (electrons/pixel), while the ensemble average of the pixel standard deviations was used to calculate the error ($\pm \frac{\sigma_x}{\sqrt{N}}$). This measurement was then repeated for several different dark exposure times. For these measurements, the gain was set to 1 and the EMCCD temperature was $-40\text{ }^\circ\text{C}$. A plot of exposure time versus dark current count is shown in Figure 9. The fitted slope gives 0.14 electrons/pixel/second which agrees with the dark current rate given in the TC253 datasheet.

3) *Read Noise*: The main source of read noise in the system arises from the charge-to-voltage conversion in the EMCCD output amplifier. Assuming that the spurious charge has been reduced to a negligible level, then for a zero second dark exposure ($P = D = 0$) at a gain of 1, Equation 4 reduces to:

$$\sigma_t = \sqrt{\sigma_r^2} = \sigma_r \quad (7)$$

so that the total noise is equal to the total read noise. The read noise of the system was measured by taking 1000 zero second exposures at a gain of 1 and calculating the standard deviation

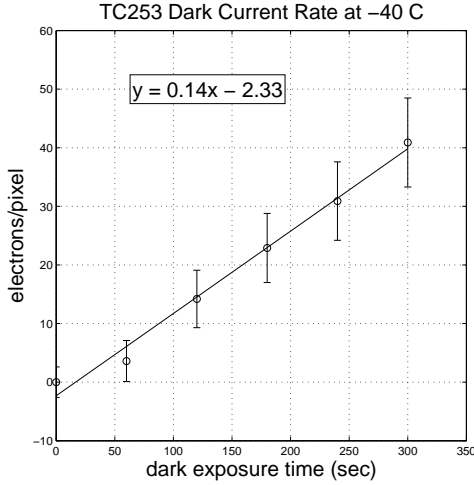


Fig. 9. A plot of dark current count (electrons/pixel) versus dark exposure time. The fitted slope gives the dark current accumulation rate for the EMCCD at -40°C .

for each pixel. The ensemble average of the pixel standard deviations over the active EMCCD area was then multiplied by the system video gain (0.57 electrons/ADU) to give a read noise of 18.2 electrons/pixel RMS. The measured read noise was lower than the read noise stated in the TC253 datasheet (29 electrons/pixel RMS) due to the 200 kHz maximum readout rate of the current ADC. Although fine for initial testing, a faster ADC will be needed to achieve video rate readout (12.5 MHz). This will increase the readout noise which is proportional to the readout speed.

4) *Spurious Charge*: Along with dark current, non-photon related electrons known as spurious charge (or clock induced charge) can be generated during the readout of the EMCCD. Spurious charge arises from the rapid inversion of the clocking potentials and tends to increase with faster readout speeds and lower temperatures [33]. Methods to reduce spurious charge include using a slow parallel-transfer from the image area to the storage area, setting the rise and fall times of the clocking pulses to about 200 ns, and using the minimum clocking potentials necessary for efficient charge transfer [26], [31]. Of these three methods, the greatest observed reduction in spurious charge for the TC253 was seen by minimizing the clocking potentials [34].

Spurious charge generation as a function of +CMG was measured for the TC253 by taking 100 zero second dark exposures for a fixed +CMG voltage. The ensemble average of the standard deviations for each pixel was then calculated and taken as the total noise (σ_t). For a zero second dark exposure ($P = D = 0$) Equation 4 can be rewritten as:

$$S = \frac{\sigma_t^2 + \sigma_r^2}{F^2 G^2} \quad (8)$$

By using σ_t from above, σ_r and G from the previous read noise and gain measurements, and knowing that $F \rightarrow \sqrt{2}$ at high gain, the spurious charge generation was calculated to be 3 to 4 electrons/pixel at gains from $500\times$ to $1000\times$. This spurious charge generation could not be further reduced by the minimizing methods listed above and appears to be an

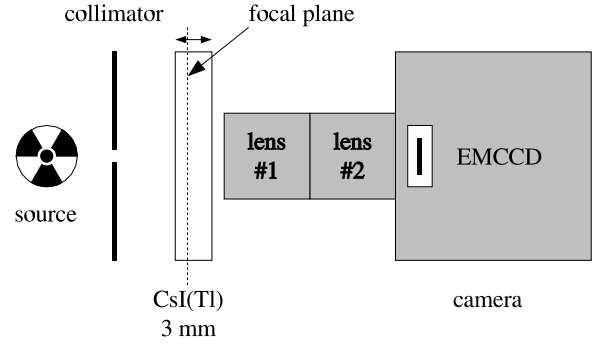


Fig. 10. A schematic of the EMCCD SPECT setup. Two lenses are used to improve the optical transfer of the scintillation light to the EMCCD. The lens focal plane can be moved through the crystal.

inherent property of the TC253, largely caused by the use of virtual-phase electrode technology [22]. This spurious charge generation is therefore the true noise floor for the TC253 chip making it incapable of single photoelectron sensitivity. Consequences of this measurement are further discussed in Section IV. As a comparison, this same measurement was done with a high-quality commercially available EMCCD camera (Princeton Instruments/Acton PhotonMAX 512B with the e2v CCD97 EMCCD) which yielded a spurious charge generation of less than 0.01 electrons/pixel.

B. Intrinsic Resolution

A schematic of the lens-coupled SPECT setup is shown in Figure 10. Two 1-inch format lenses (Schneider Xenon 0.95/25) were coupled front-to-front in order to improve the optical transfer to the EMCCD. Both lenses had an f-stop of 0.95 with the front lens focus set to infinity and the rear lens focus being adjustable. A 3 mm thick monolithic CsI(Tl) crystal was then placed 5 to 10 mm in front of the lenses so that the shallow focal plane (less than 1 mm deep) could be moved through the crystal. The two coupled lenses image a field of view (FOV) on the crystal that is approximately the same size as the image area of the EMCCD ($\approx 5\text{ mm} \times 5\text{ mm}$). When compared to a single lens imaging the same FOV, we found the optical transfer when using two lenses to be improved by a factor of two.

The intrinsic resolution (R_i) for the above setup was measured using a $30\ \mu\text{m}$ slit Tungsten collimator and a ^{99m}Tc source. The activity viewed by the slit was approximately $50\ \mu\text{Ci}$ (1.9 MBq). The line spread function for a 5 minute exposure with the gain set to $200\times$ was acquired. The acquired image and 1 mm wide line profile (taken perpendicular to the slit) are shown in Figure 11. Fitting the line spread function profile with a Gaussian distribution gave a FWHM of $110\ \mu\text{m}$ which was taken as the intrinsic resolution.

C. SPECT Images

For SPECT imaging, the Tungsten slit collimator was replaced with a single pinhole Lead collimator. The pinhole diameter was 0.5 mm with an aperture angle of 90 degrees.

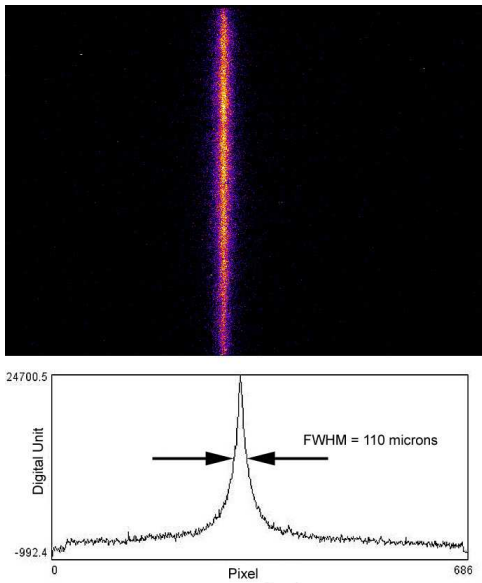


Fig. 11. The image and line profile produced by a $30\ \mu\text{m}$ slit collimator and $^{99\text{m}}\text{Tc}$ source. The exposure time was 5 minutes with a gain of $200\times$.

A small glass capillary tube was filled with aqueous $^{99\text{m}}\text{Tc}$ solution, mounted to a step motor, and placed in front of the pinhole. The 3 cm long capillary had an outer diameter of 1.5 mm, an inner diameter of 0.8 mm, and a linear activity of $10\ \mu\text{Ci}/\text{mm}$ ($0.37\ \text{MBq}/\text{mm}$). Projection data were then taken as the phantom was rotated (20 projections, 18° step) with a 3 minute exposure time for each projection. The EMCCD gain was set to $1000\times$ at a temperature of $-50\ ^\circ\text{C}$. Figure 12 shows a sample projection of the line source, with the subject FOV measuring $6.0\ \text{mm} \times 4.5\ \text{mm}$.

Image reconstruction was based on the Maximum Likelihood method (MLEM) [35] which was improved with the listmode high resolution algorithm for system matrix modeling (MLSM) [36], [37]. A convolution procedure based on the discrete Fast Fourier Transform (FFT) was used for resolution modeling. If photon scattering is neglected, the blurring component of the matrices which account for the finite resolution effects can be represented as a set of shift-invariant kernels (details given in [37], [38]). Figure 13(a) shows a transverse slice of the MLSM reconstruction for the line phantom. The total FOV ($20\ \text{mm}^3$) was subdivided into $0.25\ \text{mm}^3$ voxels. Approximately 300,000 events were reconstructed into the voxel array. A Gaussian function ($0.4\ \text{mm}$ kernel) was used to model the resolution during the 10 iterations. The FWHM of the Gaussian fitted line profile in Figure 13(b) measures $0.96\ \text{mm}$. The slight increase in the reconstructed diameter is due to the total resolution of the setup being limited by the geometric resolution (R_g) which was $\approx 1\ \text{mm}$.

IV. CONCLUSION AND DISCUSSION

A. Summary

A cost effective prototype EMCCD based gamma camera has been developed and evaluated for use in preclinical SPECT imaging. A four stage Peltier and liquid heat exchanger was used to cool the EMCCD down to $-50\ ^\circ\text{C}$. Dual $f/0.95$

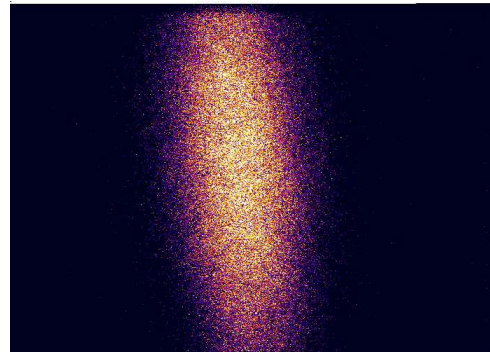


Fig. 12. A pinhole projection image of a $^{99\text{m}}\text{Tc}$ filled line phantom. The subject FOV measures $6.0\ \text{mm} \times 4.5\ \text{mm}$ with an exposure time of 3 minutes.

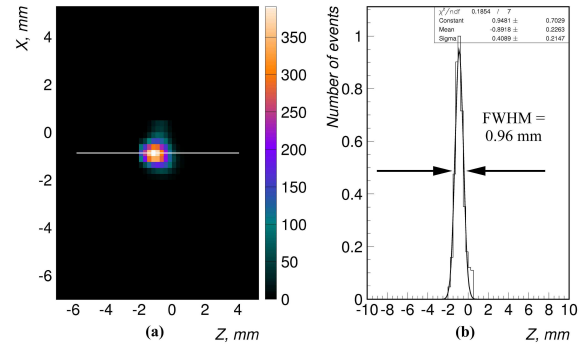


Fig. 13. SPECT reconstruction of the line source (a) with Gaussian fitted line profile (b).

lens coupling was used to image the scintillation light from a 3 mm thick monolithic CsI(Tl) crystal. A gain of over $1000\times$ was measured for the TC253 EMCCD. The dark current accumulation rate and read noise were within the specified operating range for a temperature of $-40\ ^\circ\text{C}$ and readout rate of 200 kHz. A spurious charge generation of 3 to 4 electrons/pixel was measured at high gain values. This intrinsic spurious charge could not be further reduced using established minimizing techniques and represents the noise floor for the TC253. An intrinsic resolution of $110\ \mu\text{m}$ FWHM was measured using a $30\ \mu\text{m}$ slit collimator and $^{99\text{m}}\text{Tc}$ source. Single pinhole collimation was used to take SPECT images of a small $^{99\text{m}}\text{Tc}$ line phantom. The MLEM reconstructed source size was slightly larger than the true source size due to the geometric resolution of the setup.

B. Conclusions

Although the prototype EMCCD gamma camera was capable of SPECT imaging using light integration, it was unable to perform photon counting for $^{99\text{m}}\text{Tc}$ and ^{125}I with the current optical transfer method. This can be explained by estimating the number of electrons produced in the TC253 per CsI(Tl) scintillation event. The luminosity of CsI(Tl) is 54 photons/keV with a peak wavelength of 560 nm. Approximately 10% of these scintillation photons will escape the crystal via the non-internally reflected light cone [39]. Upper limits for dual lens optical coupling efficiency (with an object to image ratio of 1:1) have been estimated to be $\approx 5\%$ [40], [41],

and the quantum efficiency of the TC253 is 35% at 560 nm. This gives $(140 \times 54 \times 0.1 \times 0.05 \times 0.35) = 13$ electrons/event for ^{99m}Tc and $(27 \times 54 \times 0.1 \times 0.05 \times 0.35) = 3$ electrons/event for ^{125}I . When these signals are spread over a 3×3 pixel area they are easily lost within the 3 to 4 electrons/pixel spurious charge noise of the TC253. Single photoelectric events were observed using a higher energy ^{137}Cs (662 keV) source where the increased number of scintillation photons results is more than 3 to 4 electrons/pixel/event. Also, when the same scintillation crystal and lens setup were used with the PhotonMAX 512B camera (e2v CCD97 EMCCD, 95% quantum efficiency at 560 nm) single photoelectric events were easily observed for both ^{99m}Tc and ^{125}I sources. These results are to be presented in a subsequent publication.

C. Further Work

One possible solution to allow photon counting with the TC253 is to improve the optical transfer of the scintillation photons to the EMCCD by using a micro-columnar CsI(Tl) crystal with a fiber-optic bundle instead of monolithic crystal with lens coupling. Fiber-optic coupling offers an order of magnitude improvement in the coupling efficiency ($> 50\%$ with a 1:1 image to object ratio) compared to lens coupling [39]. This method of photon counting has been previously established [25], [26], [42] and would allow for energy windowing, a higher intrinsic resolution, and a larger crystal FOV to be observed. Another solution could be to change from the Texas Instruments TC253 to the TC247 EMCCD. The TC247 has a higher quantum efficiency than the TC253 (50% versus 35% at 560 nm) and does not appear to be noise limited by inherent spurious charge generation [43]. Although the TC247 has a larger pixel size than the TC253 ($10 \mu\text{m} \times 10 \mu\text{m}$ versus $7.4 \mu\text{m} \times 7.4 \mu\text{m}$) it does not have a 100% fill factor which could effect the sensitivity. These two options will be explored with the goal of making our EMCCD gamma camera capable of both photon counting and energy discrimination for ^{99m}Tc and ^{125}I sources.

D. Discussion

EMCCD images formed by counting individual photoelectric events within the scintillation crystal have improved intrinsic resolutions when compared to light integration images [25]. Although resolutions of less than $100 \mu\text{m}$ have been measured, it is not yet understood how to take full advantage of this metric in preclinical SPECT imaging. For example, when using a 0.5 mm pinhole collimator with an intrinsic resolution of $100 \mu\text{m}$, the total spatial resolution is still limited by the geometric resolution of the pinhole (see Equation 1). The total resolution can be improved by reducing the pinhole diameter, but this has negative effects on the sensitivity as previously shown. Figure 14 shows a resolution plot for $R_i = d_e = 100 \mu\text{m}$. It can be seen that for $\frac{b}{a} = 1$ (no image magnification) a total resolution of about $225 \mu\text{m}$ is achieved. It can also be seen that a total resolution of less than 1 mm is still reached with $\frac{b}{a} = 5$, where the projected image on the crystal surface is *smaller* than the subject object. This means that for a subject FOV

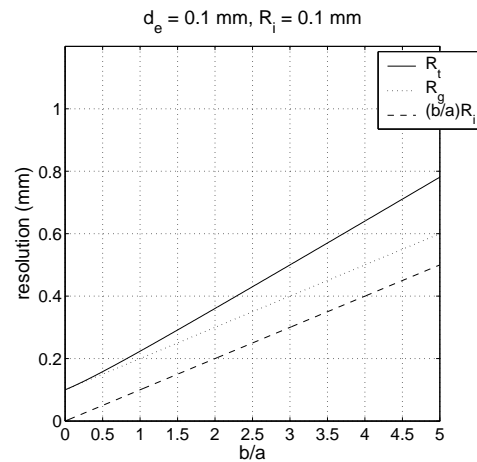


Fig. 14. A plot of R_t , R_g , and $\frac{b}{a}R_i$ versus $\frac{b}{a}$ for $d_e = 0.1 \text{ mm}$ and $R_i = 0.1 \text{ mm}$. It can be seen that a total resolution of less than 1.0 mm is still achieved at $\frac{b}{a} = 5$.

of $10 \text{ mm} \times 10 \text{ mm}$, only $2 \text{ mm} \times 2 \text{ mm}$ is needed on the crystal surface. Therefore, one hundred 0.1 mm diameter pinholes could be multiplexed onto a $20 \text{ mm} \times 20 \text{ mm}$ collimator with no image overlap on the crystal surface. Yet the combined sensitivity of these one hundred pinholes would be equivalent to a single 1.0 mm diameter pinhole. It is possible that micro-channel parallel hole [44], [45] or multiple slit [46] collimators might better use the high intrinsic resolution of an EMCCD based gamma camera to find a good balance between sensitivity and resolution in preclinical SPECT imaging.

ACKNOWLEDGMENT

The authors would like to thank Dr. Padmakar Kulkarni, Billy Smith, and Trung Nguyen of the Division of Advanced Radiological Sciences at the University of Texas Southwestern Medical Center at Dallas, and Dr. Freek Beekman and Jan Heemskerk of the Physics of Molecular Imaging and Nuclear Medicine group at the University of Utrecht for their technical assistance with this work.

REFERENCES

- [1] D. A. Weber, M. Ivanovic, D. Franceschi, S-E. Strand, K. Erlandsson, M. Franceschi, H. L. Atkins, J. A. Coderre, H. Susskind, T. Button and K. Ljunggren, "Pinhole SPECT: an approach to in vivo high resolution SPECT imaging in small laboratory animals," *J. Nucl. Med.*, vol. 35, pp. 342-348, Feb. 1994.
- [2] S. R. Cherry, "In vivo molecular and genomic imaging: new challenges for imaging physics," *Phys. Med. Biol.*, vol. 49, pp. R13-R48, Jan. 2004.
- [3] R. Weissleder and U. Mahmood, "Molecular imaging," *Radiology*, vol. 219, pp. 316-333, May. 2001.
- [4] F. J. Beekman, D. P. McElroy, F. Berger, S. S. Gambhir, E. J. Hoffman and S. R. Cherry, "Towards in vivo nuclear microscopy: iodine-125 imaging in mice using micro-pinhole," *Eur. J. Nuc. Med.*, vol. 29, pp. 933-938, Jul. 2002.
- [5] L. R. MacDonald, B. E. Patt, J. S. Iwanczyk, B. M. W. Tsui, Y. Wang, E. C. Frey, D. E. Wessell, P. D. Acton and H. F. Kung, "Pinhole SPECT of mice using the lumaGEM gamma camera," *IEEE Trans. Nuc. Sci.*, vol. 48, pp. 830-836, Jun. 2001.
- [6] K. Ishizu, T. Mukai, Y. Yonekura, M. Pagani, T. Fujita, Y. Magata, S. Nishizawa, N. Tamaki, H. Shibasaki and J. Konishi, "Ultra-high resolution SPECT system using four pinhole collimators for small animal studies," *J. Nucl. Med.*, vol. 36, pp. 2282-2206, Dec. 1995.

- [7] D. P. McElroy, L. R. MacDonald, F. J. Beekman, Y. Wang, B. E. Patt, J. S. Iwanczyk, B. M. W. Tsui and E. J. Hoffman, "Performance evaluation of A-SPECT: a high resolution desktop pinhole SPECT system for imaging small animals," *IEEE Trans. Nuc. Sci.*, vol. 49, pp. 2139-2147, Oct. 2002.
- [8] H. Kim, L. R. Furenliid, M. J. Crawford, D. W. Wilson, H. B. Barber, T. E. Peterson, W. C. J. Hunter, Z. L. Liu, J. M. Woolfenden and H. H. Barrett, "SemiSPECT: a small-animal single-photon emission computed tomography (SPECT) imager based on eight cadmium zinc telluride (CZT) detector arrays," *Med. Phys.*, vol. 33, pp. 465-474, Feb. 2006.
- [9] M. Singh and E. Mumcuoglu, "Design of a CZT based BreastSPECT system," *IEEE Trans. Nuc. Sci.*, vol. 45, pp. 1158-1165, Jun. 1998.
- [10] L. R. Furenliid, D. W. Wilson, Y. C. Chen, H. Kim, P. J. Pietraski, M. J. Crawford and H. H. Barrett, "FastSPECT II: A second-generation high-resolution dynamic SPECT imager," *IEEE Trans. Nuc. Sci.*, vol. 51, pp. 631-635, Jun. 2004.
- [11] F. J. Beekman, A. P. Colijn, B. Vastenhouw, V. M. Wiegant and M. A. F. M. Gerrits, "High-resolution emission tomography of small laboratory animals: physics and gamma-astronomy meet molecular biology," *Nucl. Instrum. Methods A*, vol. 509, pp. 229-234, Aug. 2003.
- [12] F. J. Beekman and B. Vastenhouw, "Design and simulation of a high-resolution stationary SPECT system for small animals," *Phys. Med. Biol.*, vol. 49, pp. 4579-4592, Sep. 2004.
- [13] N. U. Schramm, G. Ebel, U. Engeland, T. Schurrat, M. Béhé and T. M. Behr, "High-resolution SPECT using multipinhole collimation," *IEEE Trans. Nuc. Sci.*, vol. 50, pp. 315-320, Jun. 2003.
- [14] S. Staelens, K. Vunckx, J. De Beenhouwer, F. Beekman, Y. DAssleir, J. Nuyts and I. Lemahieu, "GATE simulations for optimization of pinhole imaging," *Nucl. Instrum. Methods A*, vol. 569, pp. 359-363, Sep. 2006.
- [15] R. Accorsi, F. Gasparini and R. C. Lanza, "A coded aperture for high-resolution nuclear medicine planar imaging with a conventional Anger camera: experimental results," *IEEE Trans. Nuc. Sci.*, vol. 48, pp. 2411-2417, Dec. 2001.
- [16] S. R. Meikle, P. Kench, A. G. Weisenberger, R. Wojcik, M. F. Smith, S. Majewski, S. Eberl, R. R. Fulton, A. B. Rosenfeld and M. J. Fulham, "A prototype coded aperture detector for small animal SPECT," *IEEE Trans. Nuc. Sci.*, vol. 49, pp. 2167-2171, Oct. 2002.
- [17] R. J. Jaszczak, J. Li, H. Wang, M. R. Zalutsky and R. E. Coleman, "Pinhole collimation for ultra-high-resolution, small-field-of-view SPECT," *Phys. Med. Biol.*, vol. 39, pp. 425-437, Mar. 1994.
- [18] F. J. Beekman, F. van der Have, B. Vastenhouw, A. J. A. van der Linden, P. P. van Rijk, J. P. H. Burbach and M. P. Smidt, "U-SPECT-I: a novel system for submillimeter-resolution tomography with radiolabeled molecules in mice," *J. Nucl. Med.*, vol. 46, pp. 1194-1200, Jul. 2005.
- [19] E. Richer, M. A. Lewis, B. Smith, X. Li, S. Seliounine, R. P. Mason and P. P. Antich, "Comparison of CsI(Tl) and scintillating plastic in a multi-pinhole/CCD-based gamma camera for small-animal low-energy SPECT," in *Small Animal SPECT Imaging*, 1st ed., M. A. Kupinski and H. H. Barrett, Ed. New York, NY: Springer, 2005, pp. 189-194.
- [20] J. Hyneczek, "CCM-a new low-noise charge carrier multiplier suitable for detection of charge in small pixel CCD image sensors," *IEEE Trans. Electron Devices*, vol. 39, pp. 1972-1975, Aug. 1992.
- [21] J. Hyneczek, "Impactron-a new solid state image intensifier," *IEEE Trans. Electron Devices*, vol. 48, pp. 2238-2241, Oct. 2001.
- [22] P. Jerram, P. Pool, R. Bell, D. Burt, S. Bowring, S. Spencer, M. Hazelwood, I. Moody, N. Catlett and P. Heyes, "The L3CCD: low light imaging without the need for an intensifier," in *Proc. SPIE*, vol. 4306, 2001, pp. 178-186.
- [23] H. O. Anger, "Radioisotope cameras," in *Instrumentation in Nuclear Medicine*, 1st ed., vol. 1, G. J. Hine, Ed. New York, NY: Academic Press, 1967, pp. 485-553.
- [24] H. O. Anger, "Scintillation camera," *Rev. Sci. Instr.*, vol. 29, pp. 27-33, Jan. 1958.
- [25] F. J. Beekman and G. A. de Vree, "Photon-counting versus an integrating CCD-based gamma camera: important consequences for spatial resolution," *Phys. Med. Biol.*, vol. 50, pp. N109-N119, May 2005.
- [26] G. A. de Vree, A. H. Westra, I. Moody, F. van der Have, K. M. Ligtoet and F. J. Beekman, "Photon-counting gamma camera based on an electron-multiplying CCD," *IEEE Trans. Nuc. Sci.*, vol. 52, pp. 580-588, Jun. 2005.
- [27] L. J. Meng, "An intensified EMCCD camera for low energy gamma ray imaging application," *IEEE Trans. Nuc. Sci.*, vol. 53, pp. 2376-2384, Aug. 2006.
- [28] J. Hyneczek and T. Nishiwaki, "Excess noise and other important characteristics of low light level imaging using charge multiplying CCDs," *IEEE Trans. Electron Devices*, vol. 50, pp. 239-245, Jan. 2003.
- [29] Corporate Publication, "On-chip multiplication gain," Roper Scientific Inc., Tucson, AZ, USA, Technical Note #14, 2003.
- [30] Corporate Publication, "The use of multiplication gain in L3Vision™ electron multiplying CCD sensors," e2V Technologies Limited, Essex, England, Low-Light Technical Note 2, Jul. 2003.
- [31] Corporate Publication, "Dark signal and clock-induced charge in L3Vision™ CCD sensors," e2V Technologies Limited, Essex, England, Low-Light Technical Note 4, Jul. 2004.
- [32] M. S. Robbins and B. J. Hadwen, "The noise performance of electron multiplying charge-coupled devices," *IEEE Trans. Electron Devices*, vol. 50, pp. 1227-1232, May 2003.
- [33] J. R. Janesick, *Scientific Charge-Coupled Devices*. Bellingham, WA: SPIE, 2001, pp. 605-654.
- [34] Corporate Publication, "Designer's guide for the TC253SPD/TX253SPD impactron CCD," Texas Instruments Inc., Dallas, TX, USA, Application Note, Mar. 2003.
- [35] L. A. Shepp and Y. Vardi, "Maximum likelihood reconstruction for emission tomography," *IEEE Trans. Medical Imaging*, vol. 1, pp. 113-122, Oct. 1982.
- [36] A. J. Reader, S. Ally, F. Bakatselos, R. Manavaki, R. J. Walledge, A. P. Jeavons, P. J. Julyan, S. Zhao, D. L. Hastings and J. Zweit, "One-pass list-mode EM algorithm for high resolution 3-D PET image reconstruction into large arrays," *IEEE Trans. Nuc. Sci.*, vol. 49, pp. 693-699, Jun. 2002.
- [37] P. Antich, R. Parkey, S. Seliounine, N. Slavine, E. Tsyganov and A. Zinchenko, "Application of expectation maximization algorithms for image resolution improvement in a small animal PET system," *IEEE Trans. Nuc. Sci.*, vol. 52, pp. 684-690, Jun. 2005.
- [38] E. Tsyganov, J. Anderson, G. Arbiq, A. Constantinescu, M. Jennewein, P. V. Kulkarni, R. P. Mason, R. W. McColl, O. K. Oz, R. W. Parkey, E. Richer, F. Rosch, S. Y. Seliounine, N. V. Slavine, S. C. Srivastava, P. E. Thorpe, A. I. Zinchenko and P. P. Antich, "UTSW small animal positron emission imager," *IEEE Trans. Nuc. Sci.*, vol. 53, pp. 243-254, Oct. 2006.
- [39] S. M. Gruner, M. W. Tate and E. F. Eikenberry, "Charge-coupled device area x-ray detectors," *Rev. Sci. Instrum.*, vol. 73, pp. 2815-2842, Aug. 2002.
- [40] S. J. Taylor, H. H. Barrett and K. Zinn, "Small animal SPECT using a lens-coupled CCD camera," in *Academy of Molecular Imaging Conference*, Orlando, Florida, Mar. 2004.
- [41] H. Liu, A. Karellas, L. J. Harris and C. J. D'Orsi, "Methods to calculate the lens efficiency in optically coupled CCD x-ray imaging systems," *Med. Phys.*, vol. 21, pp. 1193-1195, Jul. 1994.
- [42] V. V. Nagarkar, I. Shestakova, V. Gaysinskiy, B. Singh, B. W. Miller and H. B. Barber, "Fast X-ray/ γ -ray imaging using electron multiplying CCD-based detector," *Nucl. Instrum. Methods A*, vol. 563, pp. 45-48, Feb. 2006.
- [43] J. Hyneczek, personal correspondence, 2005.
- [44] G. A. Kastis, L. R. Furenliid, D. W. Wilson, T. E. Peterson, H. B. Barber and H. H. Barrett, "Compact CT/SPECT small-animal imaging system," *IEEE Trans. Nuc. Sci.*, vol. 51, pp. 63-67, Feb. 2004.
- [45] E. L. Bradley, J. Celle, S. Majewski, V. Popov, J. Qian, M. S. Saha, M. F. Smith, A. G. Weisenberger and R. E. Welsh, "A compact gamma camera for biological imaging," *IEEE Trans. Nuc. Sci.*, vol. 53, pp. 59-65, Feb. 2006.
- [46] Q. Huang and G. S. L. Zeng, "An analytical algorithm for skew-slit imaging geometry with nonuniform attenuation correction," *Med. Phys.*, vol. 33, pp. 997-1004, Apr. 2006.